RESEARCH ARTICLE

Prediction of Burr Types in Drilling of Al-7075 Using Acoustic Emission and Convolution Neural Networks

HYOJEONG KIM[1,2] **AND SEOUNG HWAN LEE**[2]
[1]Department of Mechanical Design Engineering, Hanyang University, Seoul 04763, South Korea
[2]Department of Mechanical Engineering, BK21 FOUR ERICA-ACE Center, Ansan, Gyeonggi-do 15588, South Korea

Corresponding author: Seoung Hwan Lee (sunglee@hanyang.ac.kr)

ABSTRACT The formation of exit burrs during the drilling of ductile metals such as aluminum is critical in precision manufacturing and manufacturing automation. Because drilling burrs are difficult to remove, methods to predict various burr types and/or implement burr minimization schemes that consider the various attributes of burrs must be devised. In this study, not only drilling process conditions, including feed, cutting speed, and drill diameter, but also an artificial neural network is implemented to predict the formation of burrs during the drilling of aluminum-7075, which is widely used in the aerospace and automobile industries. Based on the drilling conditions, the main exit burr characteristics, such as burr size and type, were classified experimentally. Three different types of exit burrs (uniform burrs, uniform burrs with caps, and transient burrs) were observed from the aluminum 7075 workpieces. The classification results were further analyzed using burr control charts and an empirical equation, which enables the understanding of the overall influence of the drilling conditions over the burr types. Moreover, acoustic emission (AE) sensor monitoring scheme was utilized to sample the sensitive time-series signals during drilling burr formation. Subsequently, burr types were predicted using artificial intelligence techniques, namely machining learning and deep learning. First, backpropagation (BP) neural networks were constructed using the drilling conditions and AE signals as input vectors. For a comparative prediction, a convolution neural network (CNN) was implemented to obtain spectrogram image inputs from the sampled AE data. The proposed scheme is useful in predicting drilling burr types by employing a sensitive sensor monitoring setup and advanced artificial intelligence techniques, where both prediction results are well matched with experimental results. In addition, the CNN model shows effectiveness for a commonly practiced manufacturing process as it predicts the burr types with better accuracy than the BP network model (0.9375 over 0.8571).

INDEX TERMS Drilling burr, burr type prediction, acoustic emission monitoring, AI, CNN.

I. INTRODUCTION

Machining burrs are defined as undesirable projections toward the exit portion of machined parts. Machining burrs often cause various problems during assembly and process automation of precision components, not to mention machined part quality. For instance, for ductile metals such as the Al-7075 series, which are commonly used in the

The associate editor coordinating the review of this manuscript and approving it for publication was Wei Wei.

aerospace, marine, and automobile industries due to their good mechanical properties such as a high strength–density ratio [1], burr control is essential during machining. The exit burr that occurs during drilling often generates irregularly shaped burrs such as ragged-shaped burrs and/or caps up to the drilled hole dimension. Hence, the optimal processing conditions including appropriate material properties are often applied in advance to prevent the burr generation or minimize the burr size. In general, the generated burr types are related to the machining conditions.

However, as this correlation is not necessarily explicit – that is, many variables such as the drill type/size (e.g., micro drill) can result in unexpected changes – and considering the significant amount of experimental data during machining, an efficient drilling burr analysis/prediction scheme including a burr control chart [2] is preferred. Owing to the recent development of data analysis techniques and fast computers, sensor monitoring during machining can be a valuable tool to predict real-time machining status and machining results including drilling burr formation [3]. Sensors are the main equipment for data-based condition diagnosis, and by using sensor information, an intelligent processing system can be used to determine the prognosis [4]. Therefore, several types of sensors/ sensing systems have been employed in burr formation monitoring during machining. Schleier, M. *et al* used a photodiode sensor to detect burr formation during near-infrared fiber laser cutting [5]. Rimpault *et al.* predicted the height of burrs produced during drilling for materials made of carbon fiber reinforced polymers (CFRP), titanium and aluminum alloys in terms of the thrust, torque, hole diameter, circularity, and clearance tool wear using force sensors [6]. Niknam *et al.* predicted the height of burrs produced during milling using acoustic emission sensors and force sensors [7]. Shimokura *et al.* measured the burr height using a laser displacement sensor and programmed it to debug using a robot [8]. Fitti *et al.* used laser vision sensors to detect burrs in the horizontal holes of the cylinder [9]. Peilin used machine vision and programmable logic controller (PLC) to recognize and automatically identify Edge burrs in cylindrical metal workpieces [10]. Pillai *et al.* tried to calculate the dimension of the burr height using a machine vision system [11]. Adelmann *et al.* used machine vision and artificial neural networks to classify interruption and post-cutting situations through the presence or absence of burrs [12]. The abovementioned sensor schemes have certain limitations when used in manufacturing applications, including insufficient sensitivity and difficulties in setup. Therefore, a more sensitive and practical sensor system such as an acoustic emission (AE) system is required. AE refers to the transient internal stress waves in subject material, generated by the release of strain energy from a localized source(s) such as cutting actions. The detected AE surface wave is amplified and processed to determine the exact nature of the source. AE has been applied in various precision manufacturing processes [13]. Lee *et al.* demonstrate that process control is possible through AE sensors in precision manufacturing process monitoring, such as grinding, chemical mechanical planarization (CMP) and ultra-precise diamond grinding [14].

AE also demonstrated sensitivity to transient material behaviors including burr formation [15]. Therefore, an AE sensor system can be a viable tool for in-process burr monitoring. Burrs are greatly affected by parameters such as shape, dimension, mechanical properties, cutting parameters (cutting speed, feed rate, depth of cut, etc.) of the machined part, and the cutting tool (material, shape, etc.). Therefore, monitoring a drilling burr signal acquired with an AE sensor

requires consideration of several factors. Artificial intelligence takes these factors into account and enables the prediction of burrs through the characteristic classification of sensor signals. For machining processing monitoring, artificial neural networks such as fuzzy logic, ensemble, Bayesian networks, decision and regression trees, and support vector machines are analyzed and predicted using various sensors (acoustic emission sensor, image sensor, accelerometer, etc.) [16]. Natarajan *et al.* used the teaching learning-based optimization algorithm to prevent production waste during turning [17]. Kuntoğlu *et al.* used artificial intelligence neural networks to analyze the relationship between measurement variables such as tool wear and vibration in turning [18]. Akkoyun *et al.* analyzed the correlation between the burr and slot widths formed after milling using image processing through vision technology [19]. Mikołajczyk *et al.* used ANN-based image processing to predict the tool life in turning operations [20]. Olivier *et al.* used a convolution neural network (CNN) to detect and classify faults in rotating machines [21]. Artificial neural network analysis using image processing is used in various ways, and CNN is the most commonly used among them.

The purpose of this study is to implement an in-process AE monitoring setup for drilling and predict the shape of drilling burrs by adopting artificial intelligence (AI), which is enabled by the development and implementation of advanced signal processing and computational techniques. In particular, the results obtained from using an artificial neural network (ANN) combined with backpropagation (BP), i.e., machine learning, and those obtained from using a convolution neural network (CNN), i.e., deep learning, are compared with experimental data to prove the validity of this study. This will show the adaptability of the proposed approach by connecting up-to-date AI data analysis to a specific subject (burr formation) from a commonly practiced manufacturing process.

II. DRILLING BURRS AND ACOUSTIC EMISSION MONITORING
A. BURR FORMATION MECHANISM AND BURR CLASSIFICATION
Drilling burrs are affected by many parameters, including material properties and drill geometry/ conditions [22]. Fig. 1 shows typical drilling burrs with the definitions of burr height (h) and burr thickness (t). Compared to entrance burrs, exit burrs (near the tool exit side) contributes the most to burr-related problems, as they are much larger and more complicated in shape. Among the cutting conditions, parameters that affect the burr size most significantly are feed rate and rpm (spindle speed) [22]. For instance, the rpm is associated more with the burr thickness, whereas the feed rate is associated closely with the burr height [23]. Therefore, both parameters are frequently utilized when analyzing drilling burrs [24]. According to the literature, burrs can be classified into three types based on varying the two experimental parameters:
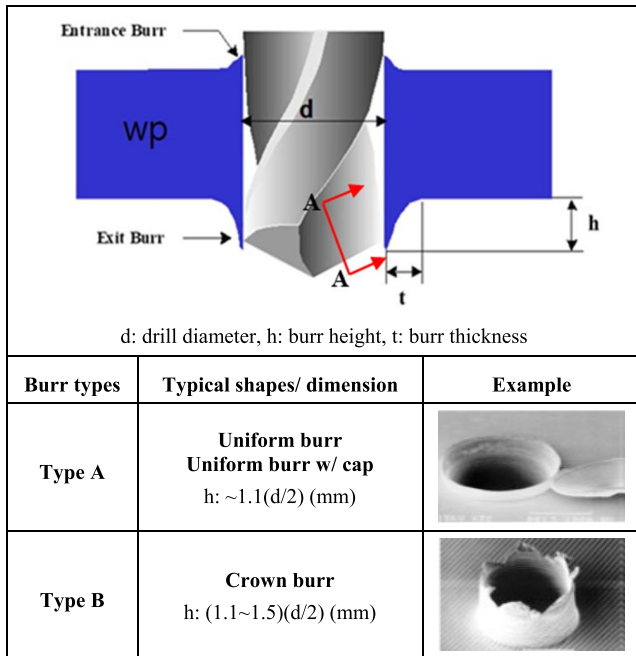
Burr types	Typical shapes/ dimension	Example
Type A	Uniform burr Uniform burr w/ cap h: ~1.1(d/2) (mm)	
Type B	Crown burr h: (1.1~1.5)(d/2) (mm)	

d: drill diameter, h: burr height, t: burr thickness

FIGURE 1. Drilling burr definitions and typical burr types.

Type I (uniform burrs), Type II (uniform burrs with cap), and Type III (crown burrs). A uniform burr has a relatively small height and thickness. Typically, it has a cap connected to the burr edge, which can either separate as the drill progresses (Type I) or remain attached (Type II). A crown burr (Type III) is owing to a larger thrust force near the center of the drilling workpiece surface, which results in irregular and ragged-shaped burrs. In this study, Type I and Type II burrs were classified as Type A burrs, and Type III burrs were designated as Type B burrs. Generally, Type B burrs are more detrimental to machining precision, assembly, and deburring than Type A burrs.

B. AE SETUP AND DRILLING BURR EXPERIMENTS

Fig. 2 shows the experimental setup comprising an AE sensor (attached to the specimen holder). AE signals were measured using a wideband UT-1000 AE sensor from PAC (Physical Acoustic Corporation), an AEDSP-32/16, a DSP board to perform high-speed signal processing for AE signal sampling, and a computer.

The signal detected by the AE sensor was amplified by 40dB by a pre-amplifier and converted into a digital signal via AEDSP32/16. The input digital signal was processed using the MISTRAS program, which controls the AEDSP-32/16 and displays data outputs and signals. The parameter settings for the AE are shown in Table. 1.

The workpieces used in the experiment were rectangular (60 × 80 × 5 mm) aluminum (Al7075, see table 2) specimens. Table.2 shows the Chemical compositions (wt: %) and mechanical properties of the workpiece.
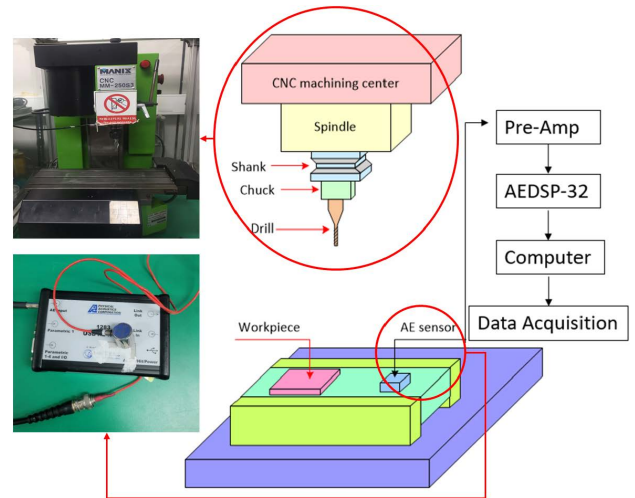

FIGURE 2. Experimental setup for drilling and AE sampling.

TABLE 1. Selected parameters and their levels.

AE sensor	UT-1000
Threshold Value	38 dB
High Pass Filter	20 kHz
Low Pass Filter	1 MHz
Sampling rate	5 MHz
Hit length	2k
Pre-amplifier	40 dB

TABLE 2. Compositions and mechanical properties of workpiece (Al 7075) [25].

Zn	Cu	Mg	Al
5.1-6.1(wt: %)	1.2-2.0(wt: %)	2.1-2.9(wt: %)	89-91.6(wt: %)
Tensile strength	Yield strength	Elastic modulus	Hardness (Brinell)
570 MPa	455 MPa	72 GPa	150 HB

FIGURE 3. Detailed dimension of drilling tool (HSS, 135° drill point angle, 61mm (L) × 33mm (SL)×3mm (D); 75mm (L) × 43mm (SL) × 4mm (D)).

Fig. 3 shows the detailed dimensions of the HSS drill used in the experiments, which were performed using two different tool diameters (3 and 4mm).

The cutting conditions were fixed through preliminary experiments considering tool specifications. Eight different feeds and three different cutting speeds were evaluated during the experiments. The cutting conditions used in the experiments are listed in table 3. Burr height measurement was performed by a contour measuring machine with an integrated digital scale detecting unit (Contracer CV-624 with the FORMPAK-1000 software), which had a resolution of 0.05 μm and a vertical measuring range of 50 mm. Measurements were repeated three times for the selected specimens.

TABLE 3. Cutting conditions.

Cutting parameter	Setup value
Feed (mm/rev)	0.01, 0.02, 0.04, 0.05, 0.1, 0.15, 0.17, 0.2
Spindle speed (rpm)	1000, 1500, 1700
Drill diameter (mm)	3, 4

The generated drilling burr types based on the experimental conditions are listed in Table 4. First, Type I (uniform burr) burrs were barely generated, except when the feed was low. Second, Type II (uniform burr with cap) burrs were formed with a gap attached to the edge of the exit hole at low feed values, similar to Type I burrs. Third, Type III (transient burr) burrs were formed around the exit and appeared in a ragged shape.

As reported earlier [3], feed is a major factor that determines the generated burr types. For example, when the feed was fixed at 0.1 mm/rev, the burr types are changed from type II to type I burr as the rotational speeds increased from 1000rpm.

A drilling burr control chart (DBCC) was utilized for the efficient analysis of burr formation based on drilling conditions [26]. For the A-A section of Fig.1, the drilling thrust force (F_t) can be expressed in terms of the drill geometry, and workpiece material parameters.

$$F_t = fd \times func(drill\ geometry\ (\kappa, H, \delta, \alpha, \phi),$$
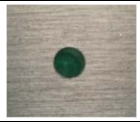$$\times\ workpiece\ material\ (k, \beta)) \quad (1)$$

Here f is feed, d is drill diameter, κ is the point angle H is the helix angle of the drill, δ is the ratio of the web thickness to the drill diameter, k is the shear strength, α is the point angel, α is the rake angle, ϕ is the shear angle, and β is the friction angle. The effective stress σ, which directly influences the burr formation mechanism can be expressed in terms of F_t and the drill diameter [27]:

$$\sigma = \frac{F_t}{A} = \frac{F_t}{d^2} \quad (2)$$

where A is the effective cutting area.

Therefore, when compiling the DBCC for a specific drill geometry and workpiece material, the normalized feed rate (f/d) is the main parameter that determines the drilling burr formation. In addition, the cutting speed reflects the cutting

TABLE 4. Drilling experimental results and burr types.

Material	TYPE A		TYPE B
	Type I Uniform burr	Type II Uniform burr with Cap	Type III Transient burr
AL7075			

Drill diameter 3 mm

Spindle speed(rpm)	Feed (mm/rev)							
	0.01	0.02	0.04	0.05	0.1	0.15	0.17	0.2
1000	II	II	II	II	I	III	III	III
1000	II	II	I	II	II	III	III	III
1000	II	II	I	I	III	III	III	I
1500	I	I	I	I	II	III	I	I
1500	I	I	1	II	III	III	III	I
1500	II	I	1	II	III	III	I	I
1700	I	I	II	I	II	I	II	II
1700	I	I	II	I	II	II	II	I
1700	I	I	I	II	I	II	II	II

Drill diameter 4 mm

Spindle speed(rpm)	Feed (mm/rev)							
	0.01	0.02	0.04	0.05	0.1	0.15	0.17	0.2
1000	II	II	II	I	III	III	III	III
1000	II	II	I	I				
1500	I	I	I	I	III	III	III	III
1500	I	I	I	I				
1700	II	II	I	I	III	III	III	III
1700	I	I	II	I				

conditions. The two parameters used in the DBCC are as follows:

$$F_n = f/d \quad S = K * d * N \quad (3)$$

where F_n is a non-dimensional feed parameter, f is the feed [mm/rev], d is the drill diameter [mm], S is the cutting speed parameter, N is the spindle speed [RPM] and K is a constant that renders the orders of the two parameters equal (10^{-5}).

Fig.4. shows the distribution of the drilling burr shapes of aluminum from experiments based on the two variables (F_n, S). As shown in the figure, the boundary between Type I and Type II is ambiguous, whereas the boundary between Type III and the rest of the burrs (Type I and II) is distinguishable. As expected, this result implies different burr formation mechanisms between the two cases (Type A and Type B).

In the DBCC shown above, the boundary line between Type A (Types I and II) and Type B (Type III) was formed via least square approximation. The fitted equation for the boundary line is expressed as follows:

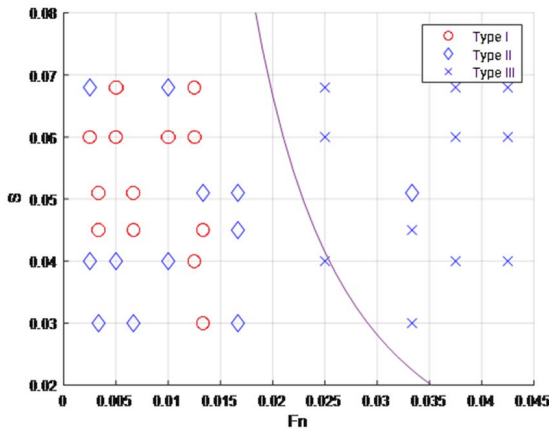$$S = 10^{-4.7934} (F_n)^{-2.1290} \quad (4)$$

FIGURE 4. Drilling burr control chart.

III. ACOUSTIC EMISSION SIGNAL ANALYSIS AND BURR PREDICTION WITH ARTIFICIAL NEURAL NETWORK

A. AE SIGNALS

From literature, AE energy levels (RMS) are known to be closely related to the tool engaging depth [28] during plastic deformation such as cutting. In addition, the friction and shearing energies dissipated in the primary, secondary and tertiary zones during cutting (drilling) are already known as major sources of AE signal generations [29].

During drilling, burrs are formed after the initial fracture as in fig.5. Regarding the AE signal processing, fracture generates a very high amplitude signal set (a sudden burst) and the signal with the highest amplitude near the end of the process can be considered as the start point of the burr formation. For that reason, after the initial fracture start point, subsequent signals were analyzed as burr generation signals (Fig.6).
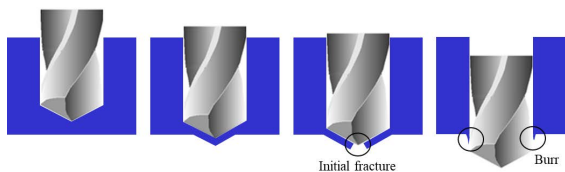

FIGURE 5. Typical drilling burr formation procedure.

Fig. 6 shows AE raw signals which were recorded during the entire drilling process, i.e., as the cutting edge enters the specimen, performs drilling, and exited from the machining end of the specimen. To correlate the AE signal with the burr shape in the experiments, both time series and frequency domain data were presented. Fig. 7 and 8 show the signals when the burrs of Type A and Type B are generated, respectively.

As explained in [30], the start position of the material fracture at the exit of the drilling is different for the two types of burrs. For instance, the fracture starts at the edge for Type A burrs, and at the center for Type B burrs. In addition, the
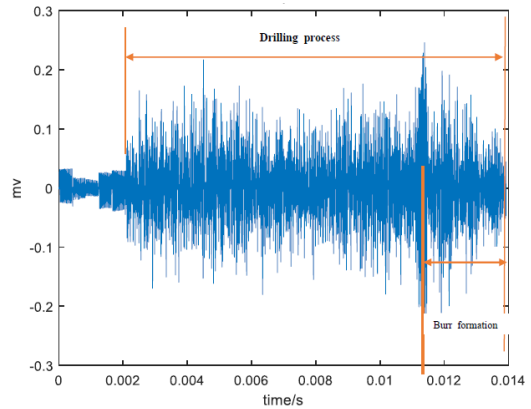

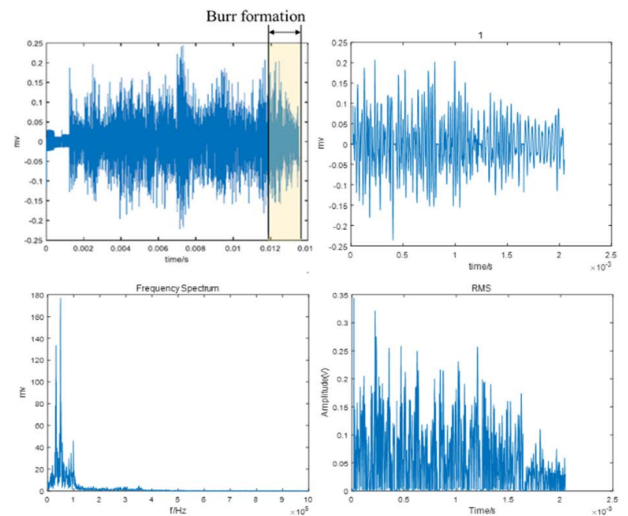**FIGURE 6.** Typical AE raw signal during drilling process.

FIGURE 7. Raw signal during drilling, raw signal, FFT and RMS during burr formation (TYPE A; 1000 rpm, f = 0.01 mm/rev, d = 3mm).

larger thrust force induces plastic deformation earlier in the process, which generates distinct AE signals. For the time domain signals, the RMS of TYPE A and TYPE B decreased and increased in general, respectively. The frequency domain signal shows that the average value of the peak frequency of TYPE A is slightly lower than that of TYPE B (40 kHz vs. 50 kHz).

Fig. 9 and 10 show the change in the RMS, AE energy, and the peak frequency of AE signal based on the feed changes. As shown in the figure, generally, the larger the drill diameter, the larger the AE RMS and AE energy values. The AE signals show a strong correlation with the generation of Type A and Type B burrs, particularly in terms of feed changes. For instance, the graphs have similarity to the burr control chart results in the previous section. In addition, changes in signal amplitudes (time series) and central frequency are shown based on the drill diameter or burr type. For more comprehensive results, more systematic analyses involving various signal processing techniques are to be conducted.
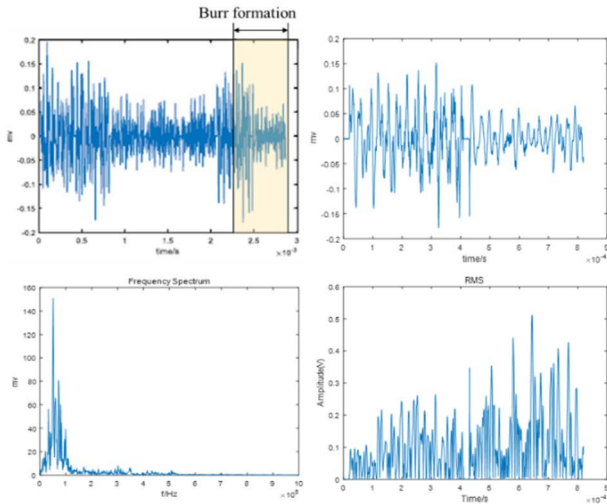
FIGURE 8. Raw signal during drilling, raw signal, FFT and RMS during burr formation (TYPE B; 1500rpm, f = 0.1mm/rev, d = 4 mm).

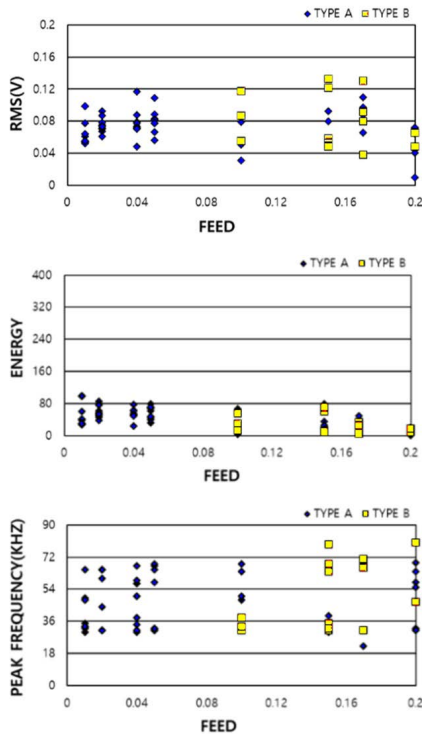**FIGURE 9.** Characteristics of AE signals from burr formation as feed changes (d = 3mm).

FIGURE 10. Characteristics of AE signals from burr formation as feed changes (d = 4mm).

B. BP LEARNING ALGORITHM (MACHINING LEARNING)

As in-process monitoring/classification is necessary for precision manufacturing and manufacturing automation, researchers have exploited signal processing combined with AI to effectively analyze the nature of processed signals and selected features [31], [32]. In this study, both machine learning (ANN with BP) and deep learning were used to analyze AE monitoring signals during burr formation. To implement both AI and in-process sensor monitoring simultaneously,
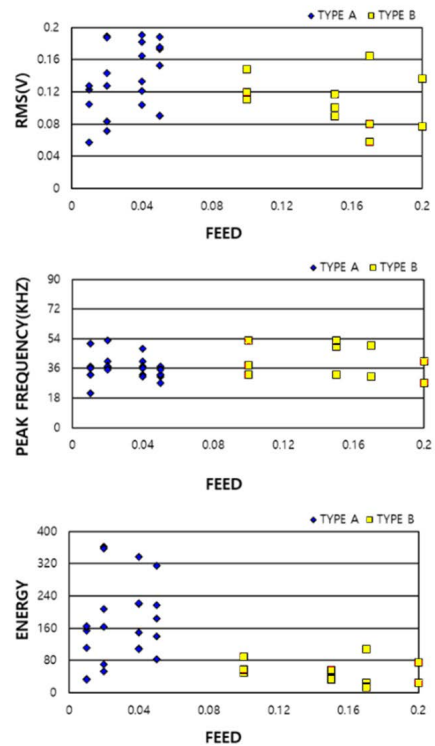
BP ANNs, whose learning and classification abilities have been proven [33], were utilized. BP is a learning algorithm that uses the error signal of the output layer to change the connection strengths between the input/ hidden layer and the hidden/output layer by backpropagating the error signal to the hidden layer. ANNs (machining learning) with BP learning algorithm have been utilized in many precision manufacturing applications including AE monitoring [34]–[37].

Six types of input vectors (features) are selected: cutting speed, feed rate, drill diameter, AE RMS, AE energy, and peak frequency. According to Ahn and Lee [3], burr type prediction using ANNs based on either cutting conditions or AE monitoring signals as input demonstrated reasonable accuracy; this validates the relevance of feature vectors and outputs (burr types). Subsequently, the selected features were fed into an ANN with BP learning as input vectors to predict the burr type during machining (i.e., six input nodes, four hidden layers, 6-12-23-13 hidden nodes, and one output node, as shown in Fig. 11). The burr shape was classified as the output layer. For the result, a value of 1 corresponds to Type A (uniform burr, uniform with gap), whereas a value of 2 corresponds to Type B (transient burr). Table 5 shows the training data set. Among a total of 108 data sets, 80% of the data set were used for training, whereas the remainder was used for burr type prediction.

Figure 12 and Table 6 show the results obtained using the BP neural network. It was observed that prediction results were generally consistent with experimental data with an accuracy of 0.857.
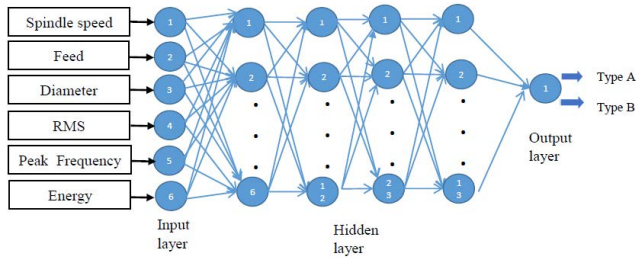
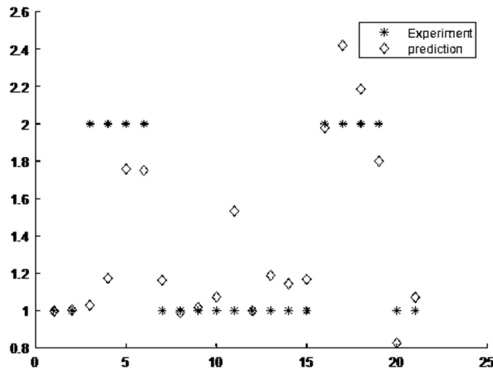**FIGURE 11.** The architecture of neural network (BP ANN).

FIGURE 12. Prediction results of burr types using BP ANN.

IV. CONVOLUTION NEURAL NETWORK WITH WAVELET PACKET TRANSFORM

In order to overcome the complicated feature selection processes arising from a significant amount of AE time series data and to enhance computational efficiency during the supervised (machine) learning processes, deep learning (CNN) with wave packet transformation (WPT) [38] is adopted. CNNs are a class of deep ANNs that use convolution instead of general matrix multiplication in at least one of their layers [39]. CNNs are primarily used for image data processing, such as image classification. In general, CNNs are more computationally efficient and accurate than fully connected networks, such as BP networks [40]. Moreover, CNNs do not require previous signal processing, including feature selection/extraction processes [41]. In addition to input and output layers, the typical layer of a convolution network typically comprises three stages: First stage: convolution (linear activation); second stage: detection, which involves nonlinear activation (e.g., the rectified linear activation function); third stage: pooling, where the output layer is modified further, and the representation is rendered approximately invariant to slight translations of the inputs [39].

In this study, a CNN technique was utilized for automatic feature extraction from AE signals during burr formation and classification of burr type using AE spectrogram images as inputs.

TABLE 5. Training data for the back propagation neural network.

No.	Peak Frequency (kHz)	Energy	RMS	Spindle Speed (rpm)	Feed (mm/ rev)	Diameter (mm)
1	49438.48	29.19629	0.053593	1000	0.01	3
2	48828.13	37.9789	0.061067	1000	0.01	3
3	48522.95	30.24927	0.054521	1000	0.01	3
4	31738.28	46.38964	0.067523	1000	0.02	3
5	31738.28	57.72164	0.075322	1000	0.02	3
6	31433.11	37.9174	0.061111	1000	0.02	3
7	30517.58	55.28964	0.07371	1000	0.04	3
8	31433.11	67.64237	0.08153	1000	0.05	3
9	31127.93	44.51926	0.066123	1000	0.05	3
10	31127.93	31.97817	0.056069	1000	0.05	3
11	48828.13	3.776916	0.030476	1000	0.1	3
12	50048.83	66.76308	0.128182	1000	0.1	3
13	30517.58	55.94213	0.11735	1000	0.1	3
14	30517.58	13.8372	0.058345	1000	0.15	3
15	34179.69	11.45231	0.05319	1000	0.15	3
16	31738.28	9.895533	0.049302	1000	0.15	3
17	67138.67	349.255	0.293323	1000	0.17	3
18	30517.58	5.856864	0.037945	1000	0.17	3
19	69580.08	34.25124	0.091864	1000	0.17	3
20	46386.72	9.332621	0.047878	1000	0.2	3
21	79345.7	17.24799	0.065324	1000	0.2	3
22	31738.28	0.348633	0.009244	1000	0.2	3
23	33569.34	99.6763	0.098933	1500	0.01	3
24	30822.75	60.91414	0.077357	1500	0.01	3
25	65002.44	98.51939	0.098474	1500	0.01	3
26	65612.79	85.92467	0.092	1500	0.02	3
27	65002.44	61.89071	0.078117	1500	0.02	3
28	65307.62	75.94878	0.08648	1500	0.02	3
29	57678.22	77.3277	0.087327	1500	0.04	3
30	34484.86	63.49055	0.079032	1500	0.04	3
31	59204.1	61.13489	0.077565	1500	0.04	3
32	32043.46	69.21532	0.082555	1500	0.05	3
33	58898.93	78.61692	0.088231	1500	0.05	3
34	32348.63	61.22863	0.077564	1500	0.05	3
35	64697.27	25.55629	0.079333	1500	0.1	3
36	37841.8	30.64136	0.086865	1500	0.1	3
37	32958.98	12.31055	0.055025	1500	0.1	3
38	67138.67	9.308065	0.047866	1500	0.15	3
39	63476.56	59.8961	0.121535	1500	0.15	3
40	78125	71.44717	0.132899	1500	0.15	3
41	31738.28	17.59732	0.065891	1500	0.17	3
42	65917.97	26.03109	0.079969	1500	0.17	3
43	67138.67	38.49806	0.097447	1500	0.17	3
44	64697.27	16.80844	0.064316	1500	0.2	3
45	58593.75	8.078986	0.044575	1500	0.2	3
46	31738.28	6.511358	0.039991	1500	0.2	3
47	35400.39	41.15498	0.063633	1700	0.01	3
48	32653.81	27.14225	0.051775	1700	0.01	3
49	33569.34	30.67995	0.055071	1700	0.01	3
50	44555.66	50.58786	0.070559	1700	0.02	3
51	31738.28	50.84424	0.07071	1700	0.02	3
52	60119.63	54.5861	0.073351	1700	0.02	3

TABLE 5. *(Continued.)* Training data for the back propagation neural network.

53	31127.93	51.30981	0.071132	1700	0.04	3
54	67138.67	49.84111	0.070047	1700	0.04	3
55	38452.15	139.1294	0.116966	1700	0.04	3
56	67140.81	40.3626	0.081351	1700	0.05	3
57	68969.73	48.15641	0.077084	1700	0.05	3
58	65917.97	71.96846	0.108612	1700	0.05	3
59	95214.84	60.84352	0.123268	1700	0.1	3
60	68359.38	61.69576	0.123819	1700	0.1	3
61	32958.98	10.39925	0.050556	1700	0.1	3
62	30517.58	34.8968	0.092659	1700	0.15	3
63	31738.28	26.09809	0.080071	1700	0.15	3
64	39062.5	79.2707	0.139942	1700	0.15	3
65	67138.67	48.70756	0.109777	1700	0.17	3
66	31738.28	31.29468	0.087798	1700	0.17	3
67	22738.28	286.9869	0.26515	1700	0.17	3
68	50048.83	20.88874	0.071694	1700	0.2	3
69	69580.08	17.38474	0.065493	1700	0.2	3
70	31738.28	21.00189	0.071768	1700	0.2	3
71	32043.46	33.55509	0.057392	1000	0.01	4
72	51879.88	33.33671	0.057245	1000	0.01	4
73	53405.76	52.53222	0.071836	1000	0.02	4
74	37231.45	70.20131	0.083048	1000	0.02	4
75	32043.46	110.2871	0.104069	1000	0.04	4
76	31536.62	149.1538	0.121155	1000	0.04	4
77	31127.93	82.51487	0.0901	1000	0.05	4
78	37231.45	362.7833	0.188697	1700	0.02	4
79	35536.62	357.848	0.187189	1700	0.02	4
80	37536.62	337.3971	0.182165	1700	0.04	4
81	36621.09	221.8679	0.190673	1700	0.04	4
82	37231.45	315.1098	0.175945	1700	0.05	4
83	35400.39	216.9633	0.188397	1700	0.05	4
84	37552.62	89.1098	0.147859	1700	0.1	4
85	92773.44	32.72709	0.090044	1700	0.15	4
86	30517.58	13.69141	0.058025	1700	0.17	4
87	31738.28	0.065334	0.004012	1700	0.2	4

A. WPT AND AE FREQUENCY DECOMPOSITION

AE raw signals from machining, including burr formation, typically incorporate transient characteristics with combinations of various dynamic events. One of the difficulties of AE signal processing is the characterization of information regarding events generated from an extensive signal dataset, particularly if both the time- and frequency-domain analyses cannot elucidate the clear relationship(s) between the process parameters and sampled signals. Because the wavelet transform (WT) provides selective resolutions for various frequency levels of time-series signals, it is well matched to acquire more organized information in the time domain at various frequency ranges. In fact, WT is particularly useful for transient events identification [42] and for extracting transient features in the signal via time-frequency localization. Hence, the WT has been utilized for AE signal analysis in manufacturing process monitoring [43]–[47].

TABLE 6. Training data for the back propagation neural network.

Input parameters						Burr type - Type A= I, II - Type B= III	
Spindle Speed (rpm)	Feed (mm/ rev)	Diameter (mm)	Energy	RMS	Peak Frequency (kHz)	Output	Real type
1000	0.04	3	23.6179	0.048	50048.8281	0.9969	I, II
1000	0.05	4	82.8572	0.090	27596.6218	1.0049	I, II
1000	0.1	4	49.8872	0.110	52490.2343	1.0285	III
1000	0.15	4	40.9349	0.101	48828.1250	1.1732	III
1000	0.17	4	108.2271	0.164	48828.1250	1.7584	III
1000	0.2	4	75.6741	0.136	26536.8437	1.7506	III
1500	0.01	4	1678.76	0.405	20446.773	1.1630	I, II
1500	0.01	4	153.9645	0.123	37537.7968	0.9892	I, II
1500	0.02	4	164.2658	0.127	40588.3789	1.0164	I, II
1500	0.02	4	208.3391	0.143	27089.8437	1.0727	I, II
1500	0.04	4	108.1057	0.133	48828.1250	1.5328	I, II
1000	0.04	3	52.2560	0.071	50049.8281	0.9985	I, II
1500	0.04	4	219.8963	0.164	28310.5468	1.1882	I, II
1500	0.05	4	140.3909	0.152	32348.6328	1.1425	I, II
1500	0.05	4	183.4886	0.173	32348.6328	1.1665	I, II
1500	0.1	4	57.9204	0.120	31738.2812	1.9802	III
1500	0.15	4	55.7852	0.117	31738.2812	2.4212	III
1500	0.17	4	25.5526	0.080	30517.5781	2.1855	III
1500	0.2	4	24.3223	0.077	39062.5000	1.7999	III
1700	0.01	4	165.171	0.127	32958.9843	0.8266	I, II
1700	0.01	4	111.1552	0.104	36621.0937	1.0718	I, II

The continuous wavelet transform (CWT) shifts through all the areas of data points, which consequently yields smooth and high-resolution outputs. For any square integrable function f(t), the CWT W (a, b) with respect to a wavelet basis ψ is defined as [48]

$$W(a, b) = \frac{1}{\sqrt{a}} \int_{-\infty}^{\infty} f(t) \overline{\psi \left(\frac{t - b}{a} \right)} dt. \quad (5)$$

Here, a is the scaling parameter (a>0), b is the shifting parameter. In addition, $\bar{\psi}$ is the complex conjugate of a wavelet ψ, which satisfies the admissibility condition [48]:

$$\int_{-\infty}^{\infty} \frac{\left| \hat{\psi}(\omega) \right|^2}{|\omega|} d\omega < \infty \quad (6)$$

where $\hat{\psi}$ denotes Fourier transform.

For the discrete wavelet transform (DWT), if we set a = 2^j, b = $k2^j$ (involute power of 2; j, k: integers), then the wavelet has the form $\psi_{j,k} = 2^{-\frac{j}{2}} \psi(2^{-j}t - k)$ and the discrete wavelet coefficients $c_{j,k}$ can be defined [48] as

$$c_{j,k} = \int f(t) \overline{\psi_{j,k}}(t) dt. \quad (7)$$

The DWT, which involves a series of low- and high-pass filters, is typically appropriate for image compression and real-time applications. The low-pass filtered signals represent the approximated shape(s) of the time series f(t), whereas the

high-pass-filtered signals reflect the signal details. In addition, DWT affords a higher computational efficiency than CWT since it reduces data redundancy [30].

As the resolution of DWT is relatively low in the high frequency region, WPT, which further decomposes the detailed information of the high frequency signals can be an alternative to the DWT. Fig. 13 illustrates the decompose tree for WPT. The WPT approach has been implemented to understand the frequency characteristics of the drilling process [49], [50]. In the present study, WPT is implemented to decompose the AE signal during drilling burr formation. WPT was applied to sampled AE signals, which are decomposed into approximate (low frequency) and detailed (high frequency) components.
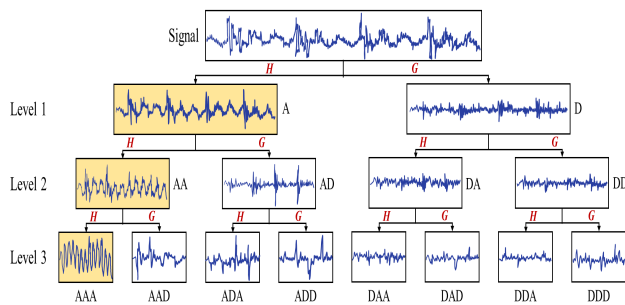

FIGURE 13. WPT decomposition tree for AE signals (H: low pass filter, G: high pass filter, A: approximation, D: Detailed) Note that DWT only considers approximation samples of each level [51].

The decomposition of the approximate and detailed components of frequency ranges was calculated using Eqs. (8) and (9), respectively [52].

$$[0, \frac{1}{2}f_s 2^{-j}] \tag{8}$$

$$[\frac{1}{2}f_s 2^{-j}, \frac{1}{2}f_s 2^{-(j-1)}] \tag{9}$$

where f_s is the sampling frequency, and 2^j is the number of components in the jth level. It shows that the AE signal is decomposed into a set of wavelet components and each component has a specific frequency range. In this work, we used MATLAB to extract wavelet packet decomposition and energy percentage functions. The wavelet energy content of each decomposed component is determined as follows [53].

$$EC_i(t) = \sum_{\tau=t_0}^{t} (f_i(\tau))^2 \tag{10}$$

$EC_i(t)$ represents the ith energy component at a certain level. The total energy of a specific level is defined as the sum of the energies of all components. The energy ratio for each component and the total energy are used to determine the energy ratio (EPC) for each component, as shown in Eq (11) [53].

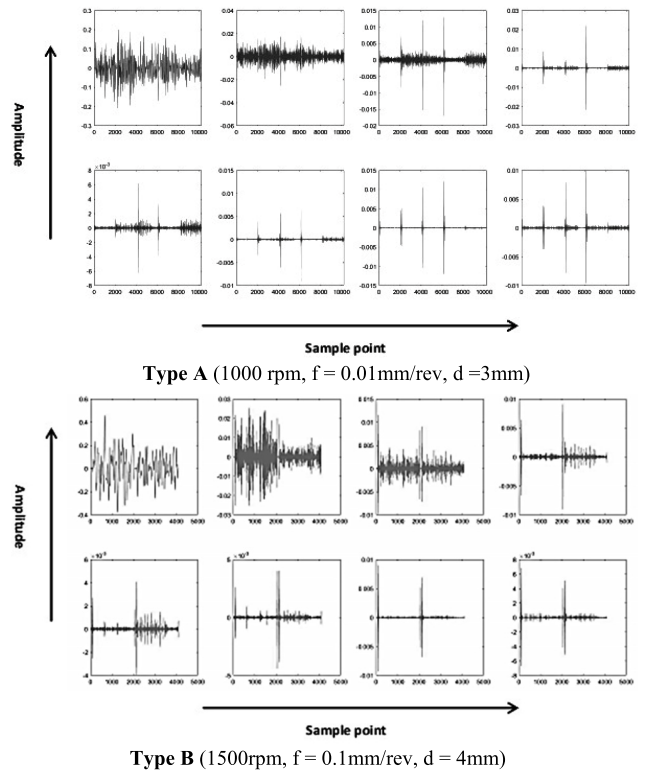$$EPC_i(t) = \frac{EC_i(t)}{EC_{Total}(t)} \quad j = 1 \dots 2^i \tag{11}$$

Type A (1000 rpm, f = 0.01mm/rev, d =3mm)

Type B (1500rpm, f = 0.1mm/rev, d = 4mm)

FIGURE 14. Typical WPT decompositions of AE signals.

TYPE A
(1000rpm0.02mm/rev3mm)
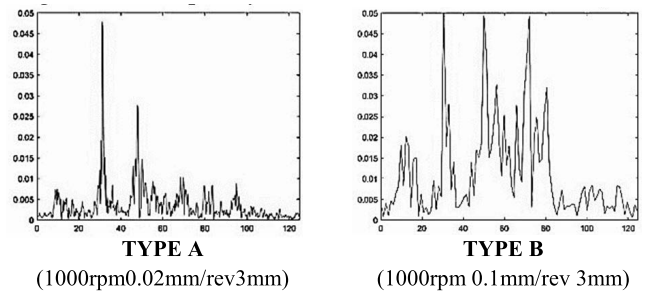
TYPE B
(1000rpm 0.1mm/rev 3mm)

FIGURE 15. Typical spectrogram inputs for the CNNs.

In this study, the optimal level was set to 3 (i = 3) for WPT (three-step decomposition involves $2^3 = 8$ components). Daubechies wavelets, known for their compactness and high adaptability to irregularly shaped signals, and Shannon-entropy ratios were used for the analysis of AE signals during drilling burr formation. AE frequency decompositions using WPT are performed on the Type A and B signals. Fig.14 shows the AE raw signals during the drilling that were subjected to wavelet transform with eight components at a frequency interval of 125kHz. The frequency range of the decomposed components is as follows. (0-125), (125-250), (250-375), (375-500), (500-625), (625-750), (750-875), (875-1000) kHz.

Table 7 shows the energy percentage at each frequency band after the wavelet transform of the raw signal. The frequency range that is the most sensitive to burr formation is
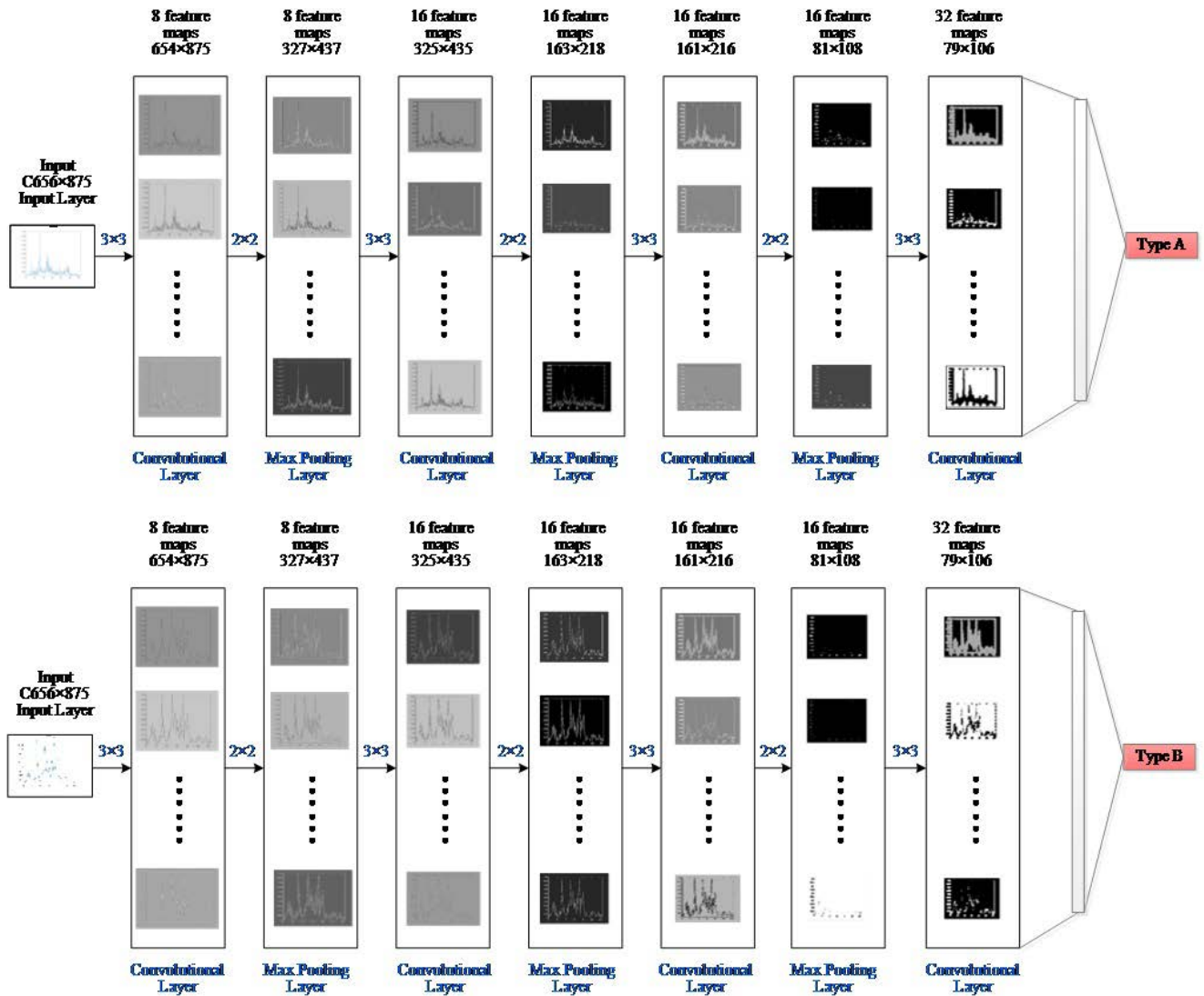
FIGURE 16. Convolutional neural network architecture for the spectrogram inputs.

indicated. As shown in the table, both Type A and Type B have the highest energy percentages at the first frequency band (0–125 kHz). Compared with Type B, the waveform energies of Type A were more concentrated in the first frequency band.

B. AE SPECTRAL INPUTS

For each process, the AE signal data were acquired at a sampling rate of 5 MHz. The AE signals obtained from the final drilling (burr formation region) were transformed into spectral images. Each image generated by the spectrogram using the first frequency band data contained 656×875 pixels.

For each process, the AE signal data were acquired at a sampling rate of 5 MHz. The AE signals obtained from the final drilling (burr formation region) were transformed into spectral images. Each image generated by the spectrogram

TABLE 7. Wavelet energy portions of each frequency band.

TYPE A								
Frequency Ranges (kHz)	-125	-250	-375	-500	-625	-750	-875	-1000
Energy % of AE waveform	97.49	1.94	0.03	0.36	0.02	0.02	0.02	0.11

TYPE B								
Frequency Ranges (kHz)	-125	-250	-375	-500	-625	-750	-875	-1000
Energy % of AE waveform	88.80	7.82	1.25	1.39	0.05	0.08	0.28	0.34

using the first frequency band data contained 656×875 pixels. Fig. 15 shows typical spectroscopic images corresponding to the two burr types. The ranges of the X-axis (frequency axis) and Y-axis (amplitude axis) were specified as 125 kHz
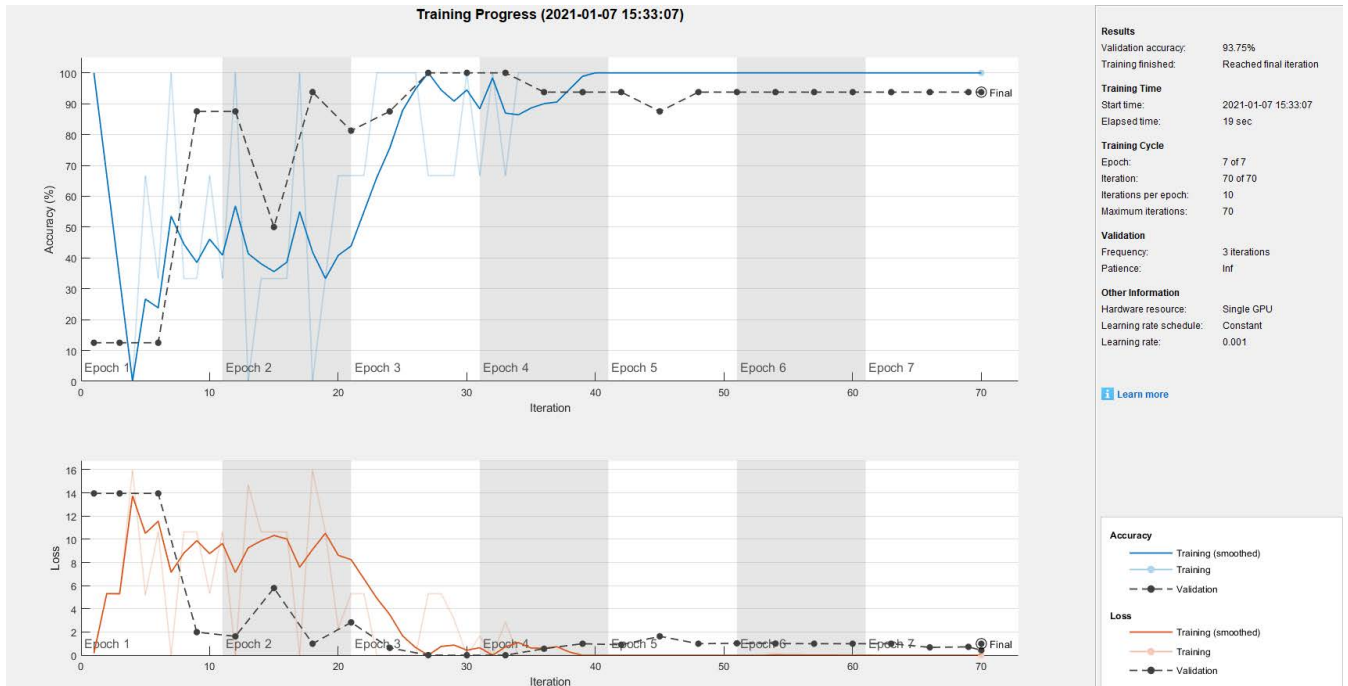
FIGURE 17. CNN training performance.

TABLE 8. Structure of CNN network model for classification.

No.	Layer name	Description
1	Image input	656×875×3 images with "zero center" normalization
2	Convolution	8 3×3convolutions with stride [1 1] and padding 'same'
3	Batchnorm	Batch normalization with 8 channels
4	Relu	Activation function of convolution layer
5	Maxpool	2x2max pooling with stride [2 2] and padding [0 0 0 0]
6	Convolution	16 3 x3convolutions with stride [1 1] and padding 'same'
7	Batchnorm	Batch normalization with 16 channels
8	Relu	Activation function of convolution layer
9	Maxpool	2x2max pooling with stride [2 2] and padding [0 0 0 0]
10	Convolution	16 3 x3convolutions with stride [1 1] and padding 'same'
11	Batchnorm	Batch normalization with 16 channels
12	Relu	Activation function of convolution layer
13	Maxpool	2x2max pooling with stride [2 2] and padding [0 0 0 0]
14	Convolution	32 3 x3convolutions with stride [1 1] and padding 'same'
15	Batchnorm	Batch normalization with 32 channels
16	Relu	Activation function of convolution layer
17	Fully connected	2 fully connected layer
18	Softmax	Activation function of convolution layer
19	Classputput	Classoutput

and 0.05 Hz, respectively. After transforming the signal into an image using a wavelet transform, it is used as input to the CNN. The network architecture and explanatory diagram are shown in Fig 16 and Table 8, respectively.

C. NETWORK SETUP AND TRAINING

The input layer picture contained 656×875 pixels. The first layer was a convolutional layer with eight feature maps, whose kernel size was 3×3. The second layer was a 2×2 max pooling layer. The third layer was a convolutional layer with 16, 3×3 feature maps and a 2×2 max pooling layer. The fourth layer was a convolutional layer with 16, 3×3 feature maps and a 2×2 max pooling layer. The fifth layer was a convolutional map comprising 32, 3×3 feature maps that were fully connected to the output layer, and the output layer contained one neuron corresponding to the shape of two burrs. The R-type and softmax functions were used as activation functions. The learning rate of the training network was 0.001, and training was performed for seven cycles. Among the AE signals in frequency band 1 (0–125 kHz), 80% of the dataset was used for the training, and the remainder was used for burr type prediction (Fig 17).

V. CONCLUSION

In this study, two AI approaches, i.e., machine learning and deep learning, were used to predict the shapes of burrs that occurred during the drilling of Al7075 via AE sensor monitoring. As the drill progressed during the cutting process, an AE signal peak was observed immediately before the tool exits the workpiece owing to changes in the cutting mechanism (exit burr generation) at the end of the cut. Hence, the AE signals after the peak were sampled and analyzed as signals relevant to the occurrence of drilling burrs.

First, we examined a BP neural network whose inputs were AE signals combined with nondimensionalized

cutting parameters. Subsequently, we examined CNNs using spectrograms as inputs after AE frequency decomposition via WPT. The conclusions obtained were as follows:

- Three different types of exit burrs (uniform burrs, uniform burrs with caps, and transient burrs) were observed in the aluminum workpieces. Uniform burrs and uniform burrs with caps were primarily observed when the feed values were less than 0.1 mm/rev, whereas transient burrs were observed at higher feeds.

- AE signals from the exit burr formation experiments show a strong correlation with generated burr types with variations of drilling parameters.

- The BP neural network model was implemented using AE signal parameters (peak frequency, RMS, and AE energy) and drilling process conditions (feed, rpm, and diameter) as inputs. The prediction results showed that the combined input results were reasonably consistent with the experimental results, with a prediction accuracy of 0.85714.

- Using WPT for the generation of AE signal spectrogram inputs, CNNs were successfully implemented for the automatic feature selection process and classification of generated burr types. Considering the satisfactory prediction accuracy (0.9375) and adaptability to practical machining processes of the proposed scheme, it can be concluded to the latter is viable for various manufacturing applications.

As the adaptability of the latest deep learning technologies to a specific aspect of a manufacturing application is shown through the presented study, the future goal is to widen the scope of the implementation to more general machining processes and features.

REFERENCES

[1] F. Toptan, A. C. Alves, I. Kerti, E. Ariza, and L. A. Rocha, "Corrosion and tribocorrosion behaviour of Al–Si–Cu–Mg alloy and its composites reinforced with B4C particles in 0.05M NaCl solution," *Wear*, vol. 306, nos. 1–2, pp. 27–35, Aug. 2013.

[2] K. Lee and D. A. Dornfeld, "Micro-burr formation and minimization through process control," *Precis. Eng.*, vol. 29, no. 2, pp. 246–252, Apr. 2005.

[3] Y. Ahn and S. H. Lee, "Classification and prediction of burr formation in micro drilling of ductile metals," *Int. J. Prod. Res.*, vol. 55, no. 17, pp. 4833–4846, Sep. 2017.

[4] M. Kuntoğlu, E. Salur, M. K. Gupta, M. Sarıkaya, and D. Y. Pimenov, "A state-of-the-art review on sensors and signal processing systems in mechanical machining processes," *Int. J. Adv. Manuf. Technol.*, vol. 116, nos. 9–10, pp. 2711–2735, Oct. 2021.

[5] M. Schleier, B. Adelmann, B. Neumeier, and R. Hellmann, "Burr formation detector for fiber laser cutting based on a photodiode sensor system," *Opt. Laser Technol.*, vol. 96, pp. 13–17, Nov. 2017.

[6] X. Rimpault, J.-F. Chatelain, J. E. Klemberg-Sapieha, and M. Balazinski, "Burr height monitoring while drilling CFRP/titanium/aluminium stacks," *Mech. Ind.*, vol. 18, no. 1, p. 114, 2017.

[7] S. A. Niknam and V. Songmene, "Burr formation and correlation with cutting force and acoustic emission signals," *Proc. Inst. Mech. Eng. B, J. Eng. Manuf.*, vol. 231, no. 3, pp. 399–414, Feb. 2017.

[8] K. Shimokura and S. Liu, "Programming deburring robots based on human demonstration with direct burr size measurement," in *Proc. IEEE Int. Conf. Robot. Autom.*, May 1994, pp. 572–577.

[9] M. Fitti, P. Castellini, N. Paone, M. Zannini, S. Zitti, M. Gambini, and P. Chiariotti, "In-line burr inspection through backlight vision," in *Proc. Int. Conf. Image Anal. Process.* Cham, Switzerland: Springer, 2019, pp. 343–351.

[10] L. Peilin, Y. Zhen, Z. Wenlong, and L. Hong, "An automatic sorting system for sorting metal cylindrical workpiece based on machine vision and PLC technology," in *Proc. 2nd Int. Conf. Robot. Autom. Eng. (ICRAE)*, Dec. 2017, pp. 446–450.

[11] A. Pillai, S. Chiddarwar, M. R. Rahul, and M. Dalvi, "Burr registration using image processing," in *Advances in Industrial Machines and Mechanisms*. Singapore: Springer, 2021, pp. 321–330.

[12] B. Adelmann and R. Hellmann, "Simultaneous burr and cut interruption detection during laser cutting with neural networks," *Sensors*, vol. 21, no. 17, p. 5831, Aug. 2021.

[13] M. Kimmelmann, J. Duntschew, I. Schluchter, and H.-C. Möhring, "Analysis of burr formation mechanisms when drilling CFRP-aluminium stacks using acoustic emission," *Proc. Manuf.*, vol. 40, pp. 64–69, Jan. 2019.

[14] D. E. Lee, I. Hwang, C. M. O. Valente, J. F. G. Oliveira, and D. A. Dornfeld, "Precision manufacturing process monitoring with acoustic emission," in *Condition Monitoring and Control for Intelligent Manufacturing*. London, U.K.: Springer, 2006, pp. 33–54.

[15] G. B. Lee, "Digital control for burr minimization in drilling," Doctoral dissertation, Dept. Mech. Eng., Univ. California, Berkeley, Berkeley, CA, USA, 1989.

[16] D. Y. Pimenov, A. Bustillo, S. Wojciechowski, V. S. Sharma, M. K. Gupta, and M. Kuntoğlu, "Artificial intelligence systems for tool condition monitoring in machining: Analysis and critical review," *J. Intell. Manuf.*, vol. 33, no. 3, pp. 1–43, Mar. 2022.

[17] E. Natarajan, V. Kaviarasan, K. M. Ang, W. H. Lim, S. Elango, and S. S. Tiang, "Production wastage avoidance using modified multi-objective teaching learning based optimization embedded with refined learning scheme," *IEEE Access*, vol. 10, pp. 19186–19214, 2022.

[18] M. Kuntoğlu, A. Aslan, D. Y. Pimenov, Ü. A. Usca, E. Salur, M. K. Gupta, T. Mikolajczyk, K. Giasin, W. Kapłonek, and S. Sharma, "A review of indirect tool condition monitoring systems and decision-making methods in turning: Critical analysis and trends," *Sensors*, vol. 21, no. 1, p. 108, Dec. 2020.

[19] F. Akkoyun, A. Ercetin, K. Aslantas, D. Y. Pimenov, K. Giasin, A. Lakshmikanthan, and M. Aamir, "Measurement of micro burr and slot widths through image processing: Comparison of manual and automated measurements in micro-milling," *Sensors*, vol. 21, no. 13, p. 4432, 2021.

[20] T. Mikołajczyk, K. Nowicki, A. Bustillo, and D. Y. Pimenov, "Predicting tool life in turning operations using neural networks and image processing," *Mech. Syst. Signal Process.*, vol. 104, pp. 503–513, May 2018.

[21] O. Janssens, V. Slavkovikja, B. Vervisch, K. Stockman, M. Loccufier, S. Verstockt, R. Van de Walle, and S. Van Hoecke, "Convolutional neural network based fault detection for rotating machinery," *J. Sound Vib.*, vol. 377, pp. 331–345, Sep. 2016.

[22] J. M. Stein, "Burr formation in precision drilling of stainless steel," Doctoral dissertation, Dept. Mech. Eng., Univ. California, Berkeley, Berkeley, CA, USA, 1995.

[23] J. M. Stein and D. A. Dornfeld, "Burr formation in drilling miniature holes," *CIRP Ann.*, vol. 46, no. 1, pp. 63–66, 1997.

[24] J. Kim and D. A. Dornfeld, "Development of a drilling burr control chart for stainless steel," *Trans.-North Amer. Manuf. Res. Inst. SME*, vol. 28, pp. 317–322, 2000.

[25] W. F. Gale and T. C. Totemeier, Eds., *Smithells Metals Reference Book*. Amsterdam, The Netherlands: Elsevier, 2003.

[26] J. Kim, S. Min, and D. A. Dornfeld, "Optimization and control of drilling burr formation of AISI 304L and AISI 4118 based on drilling burr control charts," *Int. J. Mach. Tools Manuf.*, vol. 41, no. 7, pp. 923–936, May 2001.

[27] S. Min, J. Kim, and D. A. Dornfeld, "Development of a drilling burr control chart for low alloy steel, AISI 4118," *J. Mater. Process. Technol.*, vol. 113, nos. 1–3, pp. 4–9, Jun. 2001.

[28] S. H. Lee, "Analysis of ductile mode and brittle transition of AFM nanomachining of silicon," *Int. J. Mach. Tools Manuf.*, vol. 61, pp. 71–79, Oct. 2012.

[29] J. J. B. Liu, "Monitoring the precision machining process: Sensors, signal processing and information analysis," Doctoral dissertation, Dept. Mech. Eng., Univ. California, Berkeley, Berkeley, CA, USA, 1991.

[30] S. H. Lee and D. Lee, "In-process monitoring of drilling burr formation using acoustic emission and a wavelet-based artificial neural network," *Int. J. Prod. Res.*, vol. 46, no. 17, pp. 4871–4888, Sep. 2008.

[31] J. Ranjan, K. Patra, T. Szalay, M. Mia, M. K. Gupta, Q. Song, G. Krolczyk, R. Chudy, V. A. Pashnyov, and D. Y. Pimenov, "Artificial intelligence-based hole quality prediction in micro-drilling using multiple sensors," *Sensors*, vol. 20, no. 3, p. 885, Feb. 2020.

[32] B. O. P. Soepangkat, R. Norcahyo, M. K. Effendi, and B. Pramujati, "Multi-response optimization of carbon fiber reinforced polymer (CFRP) drilling using back propagation neural network-particle swarm optimization (BPNN-PSO)," *Eng. Sci. Technol., Int. J.*, vol. 23, no. 3, pp. 700–713, Jun. 2020.

[33] Y. Bengio, I. Goodfellow, and A. Courville, "Deep learning," *Nature*, vol. 521, no. 7553, pp. 436–444, May 2016.

[34] P. Krishnakumar, K. Rameshkumar, and K. I. Ramachandran, "Machine learning based tool condition classification using acoustic emission and vibration data in high speed milling process using wavelet features," *Intell. Decis. Technol.*, vol. 12, no. 2, pp. 265–282, Mar. 2018.

[35] V. Vakharia, S. Pandya, and P. Patel, "Tool wear rate prediction using discrete wavelet transform and K-star algorithm," *Life Cycle Rel. Saf. Eng.*, vol. 7, no. 3, pp. 115–125, Sep. 2018.

[36] D. Li, Y. Wang, W.-J. Yan, and W. Ren, "Acoustic emission wave classification for rail crack monitoring based on synchrosqueezed wavelet transform and multi-branch convolutional neural network," *Struct. Health Monitor.*, vol. 20, no. 4, pp. 1563–1582, Jul. 2020.

[37] S. Mirifar, M. Kadivar, and B. Azarhoushang, "First steps through intelligent grinding using machine learning via integrated acoustic emission sensors," *J. Manuf. Mater. Process.*, vol. 4, no. 2, p. 35, Apr. 2020.

[38] Z. Liao and D. A. Axinte, "On monitoring chip formation, penetration depth and cutting malfunctions in bone micro-drilling via acoustic emission," *J. Mater. Process. Technol.*, vol. 229, pp. 82–93, Mar. 2016.

[39] I. Goodfellow, Y. Bengio, and A. Courville, *Deep Learning*. Cambridge, MA, USA: MIT Press, 2016.

[40] A. Krizhevsky, I. Sutskever, and G. E. Hinton, "ImageNet classification with deep convolutional neural networks," *Commun. ACM*, vol. 60, no. 6, pp. 84–90, 2017.

[41] D. Ibarra-Zarate, L. M. Alonso-Valerdi, J. Chuya-Sumba, S. Velarde-Valdez, and H. R. Siller, "Prediction of Inconel 718 roughness with acoustic emission using convolutional neural network based regression," *Int. J. Adv. Manuf. Technol.*, vol. 105, nos. 1–4, pp. 1609–1621, Nov. 2019.

[42] H. Suzuki, T. Kinjo, Y. Hayashi, M. Takemoto, K. Ono, and Y. Hayashi, "Wavelet transform of acoustic emission signals," *J. Acoust. Emission*, vol. 14, pp. 69–84, Jan. 1996.

[43] C. Chen, R. Kovacevic, and D. Jandgric, "Wavelet transform analysis of acoustic emission in monitoring friction stir welding of 6061 aluminum," *Int. J. Mach. Tools Manuf.*, vol. 43, no. 13, pp. 1383–1390, Oct. 2003.

[44] N. Morizet, N. Godin, J. Tang, E. Maillet, M. Fregonese, and B. Normand, "Classification of acoustic emission signals using wavelets and random forests: Application to localized corrosion," *Mech. Syst. Signal Process.*, vol. 70, pp. 1026–1037, Mar. 2016.

[45] Y. S. Ahmed, A. F. M. Arif, and S. C. Veldhuis, "Application of the wavelet transform to acoustic emission signals for built-up edge monitoring in stainless steel machining," *Measurement*, vol. 154, Mar. 2020, Art. no. 107478.

[46] C. Barile, C. Casavola, G. Pappalettera, and P. K. Vimalathithan, "Damage characterization in composite materials using acoustic emission signal-based and parameter-based data," *Compos. B, Eng.*, vol. 178, Dec. 2019, Art. no. 107469.

[47] R. Pahuja and M. Ramulu, "Surface quality monitoring in abrasive water jet machining of Ti6Al4V–CFRP stacks through wavelet packet analysis of acoustic emission signals," *Int. J. Adv. Manuf. Technol.*, vol. 104, nos. 9–12, pp. 4091–4104, Oct. 2019.

[48] R. M. Rao, *Wavelet Transforms: Introduction to Theory and Applications*. Chennai, India: Pearson, 1998.

[49] X. Li, "A brief review: Acoustic emission method for tool wear monitoring during turning," *Int. J. Mach. Tools Manuf.*, vol. 42, no. 2, pp. 157–165, 2002.

[50] H. A. Kishawy, H. Hegab, U. Umer, and A. Mohany, "Application of acoustic emissions in machining processes: Analysis and critical review," *Int. J. Adv. Manuf. Technol.*, vol. 98, nos. 5–8, pp. 1391–1407, Sep. 2018.

[51] R. Gao and R. Yan, *Wavelets: Theory and Applications for Manufacturing*. New York, NY, USA: Springer, 2010.

[52] H. Heidary, M. Ahmadi, A. Rahimi, and G. Minak, "Wavelet-based acoustic emission characterization of residual strength of drilled composite materials," *J. Compos. Mater.*, vol. 47, no. 23, pp. 2897–2908, Oct. 2013.

[53] H. Sayar, M. Azadi, A. Ghasemi-Ghalebahman, and S. M. Jafari, "Clustering effect on damage mechanisms in open-hole laminated carbon/epoxy composite under constant tensile loading rate, using acoustic emission," *Compos. Struct.*, vol. 204, pp. 1–11, Nov. 2018.

HYOJEONG KIM received the B.S. degree in mechanical engineering from Korea Polytechnic University, Ansan, South Korea, in 2017, and the M.S. degree in mechanical design engineering from Hanyang University, Seoul, South Korea, in 2019, where she is currently pursuing the Ph.D. degree with the Department of Mechanical Design Engineering. Her current research interest includes precision machining processes including monitoring system using acoustic emission.

SEOUNG HWAN LEE received the B.S. and M.S. degrees from Seoul National University, Seoul, South Korea, and the Ph.D. degree in mechanical engineering from the University of California at Berkeley, in 1996. He is currently a Professor with the Department of Mechanical Engineering, Hanyang University, Seoul. His research interests include the characterization of precision manufacturing including nano scale machining, with special emphasis on precision sensor monitoring and artificial intelligence.

• • •